Optimization of Linear Permanent Magnet Synchronous Motors for Needle-free Jet Injection

Bryan P. Ruddy* and Andrew J. Taberner
Auckland Bioengineering Institute and Department of Engineering Science
The University of Auckland, Auckland 1010, New Zealand
Email: {b.ruddy@auckland.ac.nz; a.taberner@auckland.ac.nz}
Phone: +64 9 923 2424

Jake Boyce-Bacon
The Optima Corporation
Auckland 1010, New Zealand
Email: j.boyce-bacon@theoptimacorporation.com

***Abstract*—We present a scaling model for linear permanent magnet synchronous motors applied to needle-free jet injection, a drug delivery technique that requires the generation of high fluid pressures. This model shows that either the motor stroke or the motor constant can be increased to reduce the electrical power required to perform an injection. We then present computationally efficient semi-analytical field solutions for a tubular linear synchronous motor, and use them to develop optimized motor designs for minimal jet injection power. A finite-permeability solution is developed and compared to both finite element results and a simplified infinite-permeability solution to validate the model and to establish criteria for choosing the back-iron thickness. We find that optimal jet injector motor configurations favor long stroke lengths, even at the expense of motor constant. However, designs constrained to physically reasonable motor lengths still offer an order of magnitude reduction in input power as compared to existing voice-coil-driven injection systems.**

I. Introduction

One technique for needle-free injection of drugs is jet injection, which forms a high-velocity (> 100 m/s) stream of liquid drug that can penetrate skin using nothing but its own momentum [1]. Traditionally, jet injection systems have been actuated by driving a piston using a spring or compressed gas, but this approach offers limited control of injection depth and results in a harsh injection accompanied by loud noise and occasional bruising. These effects can be mitigated by precisely regulating the jet velocity and duration under closed-loop control, using a linear electric motor to instead drive the system [2].

The actuation requirements for jet injection are very challenging for electric motors, with a pulse of high force required to pressurize the drug under near-stall conditions, and device usability considerations dictating minimization of the actuator mass. We have previously reported [3] an approach to the development of optimized voice coil actuators for this role, based on a quasi-Halbach topology. In doing so, we found that the coupling between voice coil stroke, size, and efficiency interacts with the mechanics of pressurizing a fluid in a piston-cylinder apparatus to give a scaling law for voice-coil-powered jet injectors. For a given input power, the required voice coil mass M grows faster than the injection volume V, with $M \propto V^{6/5}$. As a result, hand-held injectors delivering volumes of over 0.5 mL are not practical using voice coil actuation.

In this paper, we explore the design of linear permanent magnet synchronous motors (LPMSMs) optimized for jet injection applications. We demonstrate that the scaling laws for LPMSMs break the coupling between motor stroke and performance seen in voice coils, allowing the overall system to operate with greater efficiency. We then describe a semi-analytical electromagnetic model for tubular LPMSMs with sufficient computational simplicity and numerical stability for use in optimization, along with a dynamic model of injection to constrain the range of usable motor designs. We use these models to develop representative optimized motor designs for jet injection.

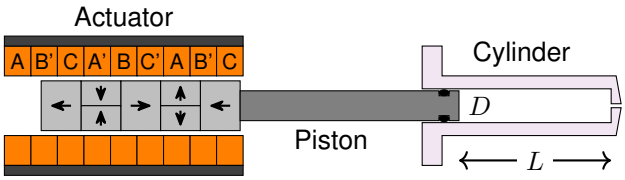

Fig. 1. A basic schematic of a synchronous-motor-driven jet injector, illustrating a schematic LPMSM with an injector ampoule. The piston diameter D and stroke L in the ampoule are illustrated.

II. Scaling Model

To review, in [3] we found the following relationship between the key physical parameters of a jet injector powered by a permanent magnet motor:

$$P = \frac{\rho^2 V^2 v^4}{4 K_m^2 L^2}, \tag{1}$$

where P is the power dissipated in the motor windings, ρ is the density of the fluid to be delivered, v is the required jet velocity, K_m is the motor constant, and L is the length of travel of the jet injector piston, as illustrated in Fig. 1. To clarify the relationship between the motor size and the motor constant, it can be non-dimensionalized as follows [4], [5]:

$$K_m = B_{\text{rem}} \hat{K}_m \sqrt{\frac{\sigma M}{\rho_c}}, \tag{2}$$

where B_{rem} is the remanance of the permanent magnets in the motor, σ is the electrical conductivity of the winding material, ρ_c is the density of the winding material, and $\hat{K}_m$ is the dimensionless motor constant.

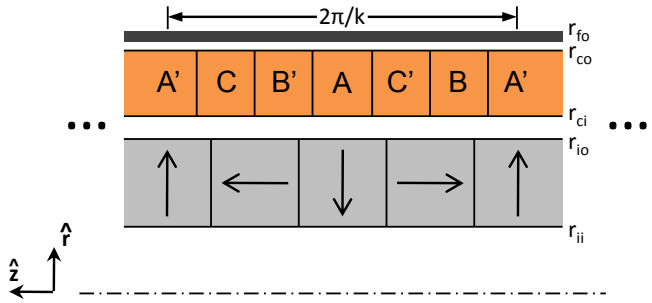

Fig. 2. This schematic illustrates the quasi-Halbach LPMSM with interior magnets and exterior back iron. The radii of the magnet, coil, and back-iron regions are shown, excluding the inner radius of the back iron r_{fi}; the structure has periodicity corresponding to a wavenumber k. (Arrows indicate the direction of magnetization in the permanent magnets.)

Unlike in the case of voice coils, for LPMSMs the dimensionless motor constant is largely independent of external motor parameters, such as mass or stroke length, instead depending on the internal proportions of the magnets and coils within each repeat unit [5], [6]. Combining (1) and (2) thus yields a final scaling relation,

$$P \propto \frac{V^2 v^4}{M L^2 \hat{K}_m^2}, \tag{3}$$

neglecting material properties. When designing the actuator, our goal is to minimize the mass M while varying the internal motor dimensions and the motor stroke L; all other parameters are set by the application.

On the face of it, this scaling relationship implies that the motor can be made arbitrarily small simply by using a very long stroke with very small repeat units of magnet and coil. In practice, the dimensionless motor constant is not completely independent of the repeat unit size; the clearance gaps between the magnets and coils do not scale, breaking scale invariance. In order to determine the limits of scale invariance, we must turn to electromagnetic modeling of the motor structure.

III. Electromagnetic Model

We will consider one particular motor topology here, the tubular LPMSM with quasi-Halbach interior magnets, slotless windings, and exterior back iron, as shown in Fig. 2. Tubular slotless topologies offer the advantages of simple mechanical construction and high copper utilization, at the expense of computational difficulties in their modeling. Our basic modeling approach is outlined in [5] and [3]: we use a Fourier series solution, with exact analytical solutions to the Poisson equation in cylindrical coordinates for the fields in radially-oriented magnets and in the coils. This formulation avoids the computational inefficiency of the standard integral formulation [7], [8], as well as the cancellation error and numerical instability exhibited by that and by other explicit analytical solutions (e.g. [9], [10]).

A. General Formulation

We analyze a motor with the repeat unit dimensions illustrated in Fig. 2. The numbers of magnet and coil repeat units employed are given by N_m and N_c, respectively. The stroke L is then given by

$$L = \frac{2\pi}{k} \left| N_m - N_c \right|, \tag{4}$$

with the motor overhung if $N_c > N_m$ and underhung if $N_c < N_m$. (Motors with the coil allowed to partially exit the magnetic field region are not considered here.) The overall length of the motor L_m is thus given by

$$L_m = \frac{2\pi}{k} \max\left(N_c,\, N_m\right). \tag{5}$$

We describe the magnetization of the permanent magnets in terms of its Fourier series decomposition,

$$\hat{M}_{rn} = \frac{4 N_{\text{seg}}}{n\pi^2} \sin\left(\frac{\pi}{N_{\text{seg}}}\right) \sin\left(\frac{n\pi\delta}{2}\right), \tag{6}$$

$$\hat{M}_{zn} = -\frac{4}{n\pi} \cos\left(\frac{n\pi\delta}{2}\right), \tag{7}$$

where $\hat{M}_{rn}$ and $\hat{M}_{zn}$ are the dimensionless radial and axial magnetizations, respectively, at odd harmonic order n, δ refers to the fraction of the magnet array occupied by radially-oriented magnets, and N_{seg} denotes the number of uniformly-magnetized segments used to approximate true radial magnetization [11].

We describe our field solutions in terms of auxiliary functions based on the modified Struve function $\mathrm{L}_\nu(x)$ and the modified Bessel functions $\mathrm{I}_\nu(x)$ and $\mathrm{K}_\nu(x)$:

$$\Lambda_\nu(x) \equiv \frac{\pi}{2}\big(\mathrm{I}_\nu(x) - \mathrm{L}_\nu(x)\big), \tag{8}$$

$$\mathcal{L}_{\mathrm{I}}(x) \equiv x\left(\Lambda_1(x)\,\mathrm{I}_0(x) - \Lambda_0(x)\,\mathrm{I}_1(x)\right), \tag{9}$$

$$\mathcal{L}_{\mathrm{K}}(x) \equiv x\left(\Lambda_1(x)\,\mathrm{K}_0(x) + \Lambda_0(x)\,\mathrm{K}_1(x)\right). \tag{10}$$

The function $\Lambda_\nu(x)$ has computationally efficient series representations [12], and only takes on values between zero and one for positive values of its argument.

The magnetic fields in free space are given by

$$B_{rn} = B_{\text{rem}}\Big(\ \hat{a}_n\,\mathrm{I}_1(nkr) + \hat{b}_n\,\mathrm{K}_1(nkr)\Big) \quad \text{and} \tag{11a}$$

$$B_{zn} = B_{\text{rem}}\Big(-\hat{a}_n\,\mathrm{I}_0(nkr) + \hat{b}_n\,\mathrm{K}_0(nkr)\Big) \tag{11b}$$

in the radial and axial directions, respectively. Determining the force produced F by integrating the Lorentz force over the coil, we find a dimensionless force constant $\hat{F}$, with

$$F = \frac{2\pi B_{\text{rem}} J_1 N_m}{k^3}\hat{F}, \tag{12a}$$

$$\hat{F} \equiv \pi\Big(\hat{a}_{1c}\hat{b}_{1m} + \hat{a}_{1m}\hat{b}_{1c}\Big). \tag{12b}$$

Here, J_1 is the magnitude of the first harmonic of the current distribution, $\hat{a}_{1m}$ and $\hat{b}_{1m}$ are magnetic field coefficients determined by matching boundary conditions for the first harmonic, and $\hat{a}_{1c}$ and $\hat{b}_{1c}$ are parameters based on the coil radii:

$$\hat{a}_{1c} = \mathcal{L}_{\mathrm{K}}(kr_{co}) - \mathcal{L}_{\mathrm{K}}(kr_{ci}), \tag{13a}$$

$$\hat{b}_{1c} = \mathcal{L}_{\mathrm{I}}(kr_{co}) - \mathcal{L}_{\mathrm{I}}(kr_{ci}). \tag{13b}$$

The length of the magnet structure is used as a reference scale for the motor size.

To find the dimensionless motor constant, we also need to non-dimensionalize the power dissipation and mass of the motor:

$$\hat{P} \equiv \frac{\sigma k^3}{2\pi N_m J_1^2} P = \frac{\pi}{2}\left((kr_{ci})^2 - (kr_{co})^2\right), \tag{14}$$

$$\hat{M} \equiv \frac{k^3}{2\pi \rho_c N_m} M. \tag{15}$$

(In calculating the motor mass, the back-iron is assumed to extend for the length of the magnet structure; i.e. a moving-coil arrangment.) In addition, we need to account for the different lengths of the coil and magnets, via a stroke length parameter y [5],

$$y \equiv \max\left(\frac{N_c}{N_m}, \frac{N_m}{N_c}\right), \tag{16}$$

as well as the coil fill factor x. The first-harmonic winding factor w for the simple block winding illustrated in Fig. 2 is given by

$$w = \frac{2N_\phi}{\pi} \sin\frac{\pi}{2N_\phi}, \tag{17}$$

where N_ϕ is the number of winding phases. The dimensionless motor constant can then be determined via

$$\hat{K}_m = w\hat{F}\sqrt{\frac{x}{y\hat{P}\hat{M}}}. \tag{18}$$

B. Infinite Permeability

The field solution for infinitely-permeable back iron has been derived in [3] in the context of voice coils:

$$b_{nm} = \hat{M}_{r1}\left(\mathcal{L}_{\mathrm{I}}(nkr_{\mathrm{io}}) - \mathcal{L}_{\mathrm{I}}(nkr_{\mathrm{ii}})\right) - \hat{M}_{z1}\left(nkr_{\mathrm{io}}\,\mathrm{I}_1(nkr_{\mathrm{io}}) - nkr_{\mathrm{ii}}\,\mathrm{I}_1(nkr_{\mathrm{ii}})\right), \tag{19a}$$

$$a_{nm} = b_{nm}\frac{\mathrm{K}_0(nkr_{fi})}{\mathrm{I}_0(nkr_{fi})}, \tag{19b}$$

for any harmonic order n.

In order to constrain the thickness of the back iron, its thickness can be set to yield a desired maximum flux density within it. Neglecting the magnetic field produced by the applied current, the maximum flux density B_{sat} can be found by integrating the field (including all harmonics) at the iron's inner surface in the axial direction over a length equal to one quarter of the period, then dividing by the cross-sectional area of the back iron:

$$B_{\mathrm{sat}} = \frac{r_{fi}B_{\mathrm{rem}}}{r_{fo}^2 - r_{fi}^2}\sum_{n=1}^{\infty}\frac{2\sin\left(\frac{n\pi}{2}\right)}{nk}\big(a_{nm}\,\mathrm{I}_1(nkr_{fi}) + b_{nm}\,\mathrm{K}_1(nkr_{fi})\big). \tag{20}$$

This equation can be readily inverted to find the required outside diameter for a particular inside diameter and flux density.

C. Finite Permeability

Semi-analytical modeling of finite-permeability effects in slotless tubular LPMSMs does not appear to have been explored extensively. Wang and Howe [13] describe an iterative technique for slotted motors based on the discrete reluctances of the teeth and back-iron, wherein a fictitious air gap is added between the magnets and stator to account for saturation. Meessen et al. [14] describe a more complex model that accounts for finite permeability in uniform layers, but is too computationally expensive to use with nonlinear materials.

Here, we solve for the fields in a tubular LPMSM with saturable iron, subject to the assumption that the relative permeability μ is uniform within the iron. The field coefficients can be found by matching boundary conditions in the usual manner, with some effort, and are given in (21). The quantities $\hat{a}'_{nm}$ and $\hat{b}'_{nm}$ are the field coefficients within the iron itself. We then assume that the point of maximum flux density B_{max} within the iron lies on its inner surface, one quarter period from the center of a radial magnet:

$$B_{\mathrm{max}} = B_{\mathrm{rem}}\sum_{n=1}^{\infty}\left(-\hat{a}'_{nm}\,\mathrm{I}_0(nkr_{fi}) + \hat{b}'_{nm}\,\mathrm{K}_0(nkr_{fi})\right)\sin\left(\frac{n\pi}{2}\right). \tag{22}$$

Using the formula for B_{max}, and a curve fit describing the nonlinear behavior of the iron, iteration is performed via Brent's method until the permeability converges. The field coefficients can then be used with (12b) to determine the motor performance.

$$\hat{b}_{nm} = \hat{M}_{rn}\left(\mathcal{L}_{\mathrm{I}}(nkr_{io}) - \mathcal{L}_{\mathrm{I}}(nkr_{ii})\right) - \hat{M}_{zn}\left(nkr_{io}\,\mathrm{I}_1(nkr_{io}) - nkr_{ii}\,\mathrm{I}_1(nkr_{ii})\right) \tag{21a}$$

$$\hat{b}'_{nm} \equiv \frac{\mu\hat{b}_{nm}}{nkr_{fi}}\Bigg[\mathrm{I}_1(nkr_{fi})\,\mathrm{K}_0(nkr_{fi}) + \mu\,\mathrm{I}_0(nkr_{fi})\,\mathrm{K}_1(nkr_{fi}) - \frac{(\mu-1)^2\,\mathrm{I}_1(nkr_{fi})\,\mathrm{I}_0(nkr_{fi})\,\mathrm{K}_1(nkr_{fo})\,\mathrm{K}_0(nkr_{fo})}{\mu\,\mathrm{I}_1(nkr_{fo})\,\mathrm{K}_0(nkr_{fo}) + \mathrm{I}_0(nkr_{fo})\,\mathrm{K}_1(nkr_{fo})}\Bigg]^{-1} \tag{21b}$$

$$\hat{a}'_{nm} \equiv -\hat{b}'_{nm}\frac{(\mu-1)\,\mathrm{K}_0(nkr_{fo})\,\mathrm{K}_1(nkr_{fo})}{\mu\,\mathrm{I}_1(nkr_{fo})\,\mathrm{K}_0(nkr_{fo}) + \mathrm{I}_0(nkr_{fo})\,\mathrm{K}_1(nkr_{fo})} \tag{21c}$$

$$\hat{a}_{nm} = \frac{nkr_{fi}}{\mu}\left[\hat{a}'_{nm}\left(\mu\,\mathrm{I}_1(nkr_{fi})\,\mathrm{K}_0(nkr_{fi}) + \mathrm{I}_0(nkr_{fi})\,\mathrm{K}_1(nkr_{fi})\right) + \hat{b}'_{nm}\,(\mu-1)\,\mathrm{K}_1(nkr_{fi})\,\mathrm{K}_0(nkr_{fi})\right] \tag{21d}$$

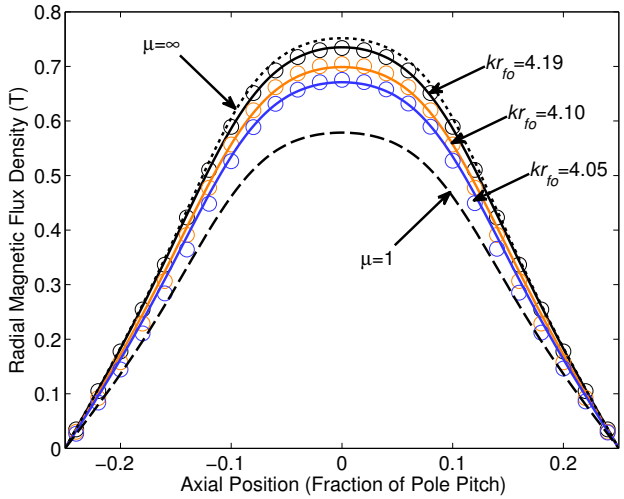

Fig. 3. The unloaded radial flux density at the mean coil radius ($kr = 3.45$) is shown for motors with $kr_{ii} = 0.86$, $kr_{io} = 3.0$, $kr_{ci} = 3.03$, $kr_{co} = 3.87$, $kr_{fi} = kr_{fi} = 3.91$, and $\delta = 0.41$, for three different iron thicknesses, $kr_{fo} = 4.19$, $kr_{fo} = 4.10$, and $kr_{fo} = 4.05$. The dashed lines represent the field in the absence of iron, the dotted lines show the field with infinitely-permeable iron, the solid lines indicate the field according to the finite-permeability model using 1018 steel, and the circles show the field according to an ANSYS finite element model. (Only one half-period is shown, due to symmetry.)

TABLE I
COMPARISON OF IRON MODELS.

B_{sat}	$\hat{K}_\infty$	$\hat{K}_{\text{finite}}$	$\hat{K}_{\text{FEA}}$	$\hat{F}_\infty$	$\hat{F}_{\text{finite}}$	$\hat{F}_{\text{FEA}}$
2 T	0.274	0.270	0.260	6.384	6.278	6.215
3 T	0.282	0.262	0.254	6.384	5.928	5.919
4 T	0.286	0.255	0.246	6.384	5.677	5.652
No Iron	N/A	0.230	N/A	N/A	4.880	N/A

D. Model Validation

The results from the finite-permeability model were compared to results from the infinite-permeability model as well as those from a unity-permeability (ironless) model. Matching geometries were also examined in ANSYS using identical nonlinear material properties for 1018 steel [15]. (In both cases, the radial magnets were assumed to behave ideally, rather than as segmented uniform magnets.) For simplicity, the fill factor x and the stroke length parameter y were both set equal to 1.

Fig. 3 shows a comparison of the model and FEA results for three different requested iron flux densities in a representative motor configuration; $kr_{fo} = 4.19$ corresponds to $B_{\text{sat}} = 2\,\text{T}$, $kr_{fo} = 4.10$ to $B_{\text{sat}} = 3\,\text{T}$, and $kr_{fo} = 4.05$ to $B_{\text{sat}} = 4\,\text{T}$. While the designs requesting saturation fluxes well in excess of the real saturation flux density of iron do not match the infinite-permeability model, as would be expected, the fully-saturated iron still contributes strongly to the performance. The magnetic field profile predicted by the analytical model matches the FEA result closely, though it possesses a slightly broader and lower peak.

Table I gives the dimensionless motor constant and dimensionless force constant predicted by each of the models; the dimensionless motor constant is calculated from the first harmonic of the current and field, while calculation of the dimensionless force constant uses the full field and current waveform (to the 99th harmonic), with a single-phase winding. For this motor configuration, the best performance is obtained when the iron is not saturated, unlike the situation for voice coils [3]. With unsaturated iron, the infinite-permeability model closely matches the results from the finite-permeability model, while exhibiting significantly faster computation.

IV. Design Optimization

Using the infinite-permeability electromagnetic model, we optimized the motor design by minimizing the power dissipation P, calculated via (1), (2), and (18), while holding motor mass M fixed. The value for B_{sat} was chosen as 2 T based on the results from the finite permeability model. A fill factor of 62 % was assumed for the coil, the radial magnets were presumed to be made from 4 segments, and the back iron was assumed to be made from plain 1018 steel. The back-iron thickness was calculated using 11 harmonics of the magnetic field, while the force constant was calculated from the first harmonic alone.

To avoid cogging force problems and to reduce the moving mass, we examined a moving-coil configuration, with the back-iron extending the full length of the magnet array. A small number of geometric constraints were therefore applied to reflect practical design issues: clearance gaps of 0.5 mm between the magnet and coils and 0.1 mm between the coils and back iron were required to allow for coil support and movement, and the minimum iron thickness was restricted to 0.25 mm to leave it with sufficient mechanical strength.

To reduce coupling between the radial dimensions during optimization, the radial thicknesses of the coil $t_c = r_{co} - r_{ci}$ and of the magnets $t_m = r_{io} - r_{ii}$ were used rather than r_{io} and r_{co}. The wavenumber k was used to non-dimensionalize all other parameters, leaving a total of seven free parameters for optimization: N_c, N_m, kr_{ii}, kt_m, kt_c, δ, and k. Note that N_c and N_m are also subject to integer constraints, as only half-integer multiples of the pole pitch make sense as motor lengths.

Optimization was carried out separately for all combinations of N_c and N_m up to 50 pole pitches. At each combination, the remaining parameters were optimized via constrained nonlinear minimization, using the interior point algorithm. In all cases, the motor mass was constrained to a fixed value of 250 g; optimization was also performed with an additional constraint on the overall length of the motor L, fixing it to 20 cm. To provide a relevant scale for the objective function P, it was calculated for an ampoule volume V of 1 mL and a jet velocity v of 200 m/s, delivering a fluid with a density of 1000 kg/m^3.

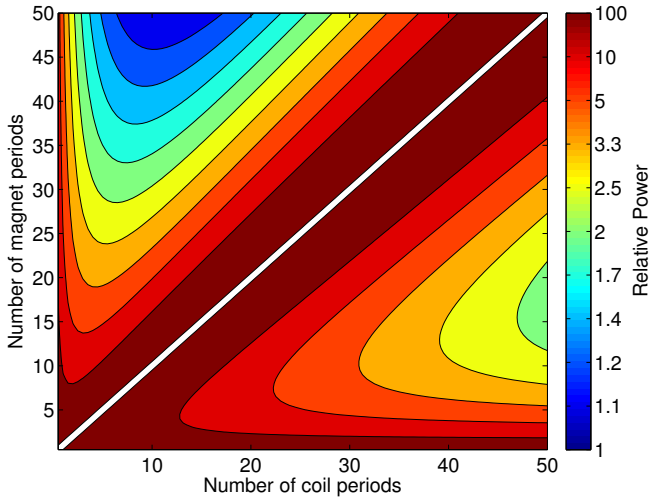

Fig. 4. A map of the performance of the optimum motor geometry at each possible combination of N_c and N_m; overhung motors lie to the lower right, while underhung motors lie on the upper left.

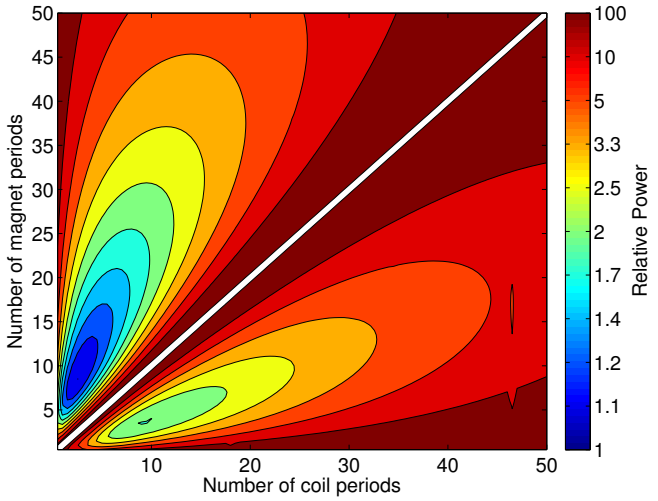

Fig. 5. A map of the performance of the optimum motor geometry at each possible combination of N_c and N_m, with the total motor length limited to 20 cm.

A. Unconstrained Optimization

The outcome of optimizing the infinite-permeability model for jet injection, with $B_{\text{sat}} = 2\,\text{T}$, is shown in Fig. 4. Each individual design optimization took under one second to complete, with all 9900 combinations of magnet and coil lengths analyzed in two hours using one core of a 2.67 GHz Intel Xeon W3520 processor. The results show that underhung motors offer superior performance to overhung motors, despite the greater mass per unit length of the magnet array and back iron, and likely due to full utilization of the copper.

The optimum configuration lies outside the search space in N_c and N_m, indicating that the penalty carried by the finite, fixed clearance gaps does not outweigh the performance improvement offered by lengthening the stroke, even for extreme aspect ratios. The optimum design within the search space has an impractical length of 1.27 m, with $N_m = 50$, $N_c = 11$, $2\pi/k = 25.5\,\text{mm}$, solid magnets with outside diameter 5.0 mm, a coil 1.5 mm thick, back-iron 0.4 mm thick, and $\delta = 0.115$; however, the objective function reaches a meager 30 W. (While true radial magnets are impossible to fabricate as solid disks, pseudo-radial magnets composed of uniformly-magnetized wedges can be built in this configuration without major difficulties.) According to the model in [3], a voice coil of the same mass would instead reach an objective function value of 56 kW, three orders of magnitude higher.

B. Additional Constraints

Given that the overall optimization problem proved to be underconstrained, we also explored the parameter space with an additional constraint on the overall motor length, restricting the longer of the magnet or coil arrays to be 200 mm long. The result of this process is shown in Fig. 5; the shape of the performance landscape has radically changed, now with optimal overhung and underhung designs. The global optimum, at 470 W, is the underhung motor with $N_m = 8.5$ and $N_c = 2.5$, which has $2\pi/k = 23.5\,\text{mm}$, solid magnets with an outside diameter of 13.4 mm, $t_c = 2.1\,mm$, back-iron 0.9 mm thick, and $\delta = 0.277$. The aspect ratio of the optimized motor is illustrated in Fig. 6, with its electromagnetic repeat unit illustrated in Fig. 7. Despite the performance penalty from the constrained length, this motor still requires two orders of magnitude less power than a voice coil of similar mass. There is some freedom to choose designs near this optimum; for instance, motors with N_c ranging between 2 and 3.5 pole pitches and N_m from 7 to 11 pole pitches require within 5 % of the optimal power.

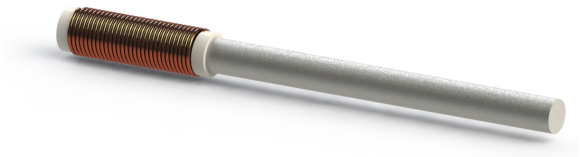

Fig. 6. A cartoon view of the optimized 200 mm motor design, illustrating the relative lengths and diameters of the coil and magnet array. (The back iron is omitted for clarity.)

We investigated a variety of more natural constraints and possible alternative objective functions, but none were sufficient to create an optimum configuration of reasonable size. Piston friction serves to make power proportional to L^{-1} for longer motors, rather than L^{-2}, but does not dominate until meter-scale lengths. Including an estimate of the mass of the support structures connecting the coil to the piston of the ampoule in the motor mass reduces the advantage of extreme stroke lengths, but does not change the shape of the optimization landscape.

C. Discussion

This optimization process focused strongly on the minimization of copper losses for high-level system design. Because

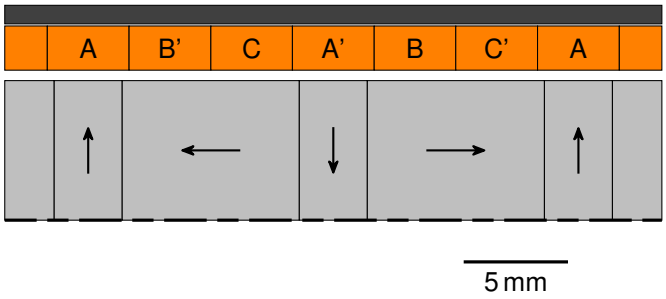

Fig. 7. A diagram of a cross-section of one pole pitch of the optimized 200 mm motor design. (The magnets extend up to the centerline.)

the windings were treated as regions of constant current density, terminal parameters (e.g. resistance, inductance, or force constant) were not directly considered. Jet injection requires a bespoke motor drive for safety, control, and packaging reasons, and there is thus considerable latitude for choosing the coil winding and drive voltage to work together.

For example, consider the constrained 200 mm motor, acting upon an ampoule with an orifice 200 μm in diameter to generate a 200 m/s jet. The motor is thus required to supply a force of 140 N at a speed of 0.9 m/s to perform an injection. Neglecting reactive impedance, winding each coil group with 3 layers of 22.5 AWG wire yields a phase resistance of 0.23 Ω, a fill factor of 53 %, and a line-line voltage during injection of 20 V, including 4 V of back-EMF. This might be suitable for a device powered directly from a lithium-ion battery. If 11 layers of 33.5 AWG wire are used instead, an improved fill factor of 58 % is possible, and the phase resistance of 41 Ω and line-line voltage of 254 V (including 51 V of back-EMF) might be suitable for a system powered from photoflash capacitors. The synchronous frequency for this motor during an injection is 38 Hz, so the effects of the unmodeled reactive impedance should be small.

While it would be impractical to build or operate the unconstrained motor design, it is instructive to examine its terminal parameters for an example winding. The unconstrained motor would need to supply 20 N at 6.2 m/s during an injection. If wound with 3 layers of 25.5 AWG wire, it would have a fill factor of 54 % and require a line-line voltage of 46 V, of which 36 V would be the back-EMF. The reactive impedance and dynamic losses of this motor would be expected to be significant, given its synchronous frequency of 240 Hz.

An additional consideration for very long motors is the effort required to accelerate the coil to injection velocity. To avoid waste of drug at the onset of the injection, the system should reach the target velocity within 10 ms. Assuming a constant acceleration, the unconstrained motor requires three times the force demanded by the fluid pressure during the injection to reach a target velocity of 200 m/s in time. The 200 mm motor, in contrast, instead only requires 4 % of the injection force for acceleration. However, the injection lasts considerably longer than 10 ms: a typical profile might call for 10 ms at a jet velocity of 200 m/s followed by 600 ms at 50 m/s. The contribution of the acceleration to the overall energy consumed by the motor thus remains relatively small.

Cost is also an important consideration, especially for devices used in home health care. For motors in this size range, the cost of the magnet material itself is almost inconsequential, but the cost of manufacture will scale with the number of individual magnet segments required to build the array. The 200 mm motor proposed here requires 17 axially-magnetized disc magnets and 68 radially-magnetized sector magnets, for a total of 85 individual magnets. By comparison, a voice coil motor with the same magnetic topology [3] uses only 6 magnet segments. Roughly speaking, then, a practical synchronous motor of comparable mass to a voice coil will have a manufacturing cost one order of magnitude higher, but consume two orders of magnitude less power during an injection. While the price is high, controlled jet injection of milliliter-scale volumes using a hand-held device is impractical at the power required for a voice coil, and the combined force, linear speed, and control bandwidth requirements are incompatible with conventional rotary drive solutions.

V. Conclusion

By optimizing the design of a LPMSM for use in jet injection, we have shown that its use allows for drastic reductions in the power required compared to a voice coil actuator. The next step will be the construction of a prototype motor and its incorporation into an injection system to validate this approach and exploit the efficiency gain. Particularly large efficiency gains are possible if the motor is allowed to be very long, but the hand-held nature of jet injection devices makes this impractical. It may be the case that there are creative packaging strategies for the motor to allow the use of long stroke lengths; the benefits of doing so are large enough that this should be an avenue for further investigation.

The performance objective for jet injection can also be more broadly construed as the objective for any low-speed fluid pumping application. These results are thus also applicable to the design of actuators for free-piston refrigeration compressors and hydraulic pumps, particularly if the model can be extended to describe dynamic performance.

This optimization was enabled by a computationally-efficient, exact semi-analytical magnetic field solution. This formulation of the field solution can also be used to develop tractable models for the dynamic performance of this class of LPMSM, including loaded and unloaded losses due to eddy currents and (more approximately) hysteresis. Future modeling efforts will be aimed at analyzing these dynamic effects, as well as end effects and at the application of this method to other tubular motor configurations.

Acknowledgment

This work was supported in part by the University of Auckland Faculty Research Development Fund and by the MedTech Centre of Research Excellence.

REFERENCES

[1] S. Mitragotri, "Current status and future prospects of needle-free liquid jet injectors," *Nat. Rev. Drug Discovery*, vol. 5, pp. 543–548, Jul. 2006.

[2] A. Taberner, N. C. Hogan, and I. W. Hunter, "Needle-free jet injection using real-time controlled linear Lorentz-force actuators," *Med. Eng. Phys.*, vol. 34, pp. 1228–1235, 2012.

[3] B. P. Ruddy, I. W. Hunter, and A. J. Taberner, "Optimal voice coil actuators for needle-free jet injection," in *36th Annu. Int. Conf. IEEE Engineering in Medicine and Biology Society (EMBC)*, Chicago, IL, 2014, pp. 2144–2148.

[4] B. Hannaford, P.-H. Marbot, P. Buttolo, M. Moreyra, and S. Venema, "Scaling of direct drive robot arms," *Int. J. Rob. Res.*, vol. 15, no. 5, pp. 459–472, 1996.

[5] B. P. Ruddy and I. W. Hunter, "Design and optimization strategies for muscle-like direct-drive linear permanent-magnet motors." *Int. J. Rob. Res.*, vol. 30, no. 7, pp. 834–845, 2011.

[6] O. Cugat, J. Delamare, and G. Reyne, "Magnetic micro-actuators and systems (MAGMAS)," *IEEE Trans. Magn.*, vol. 39, pp. 3607–3612, Nov. 2003.

[7] I. Boldea, *Linear Electric Machines, Drives, and Maglevs Handbook*. Boca Raton: CRC Press, 2013.

[8] J. Wang, G. W. Jewell, and D. Howe, "A general framework for the analysis and design of tubular linear permanent magnet machines," *IEEE Trans. Magn.*, vol. 35, pp. 1986–2000, May 1999.

[9] Wijono, H. Arof, and H. Ping, "Analysis of magnetic field distribution of a cylindrical discrete halbach permanent magnet linear generator," *IET Electr. Power Appl.*, vol. 4, no. 8, pp. 629–636, 2010.

[10] L. Yan, L. Zhang, T. Wang, Z. Jiao, C.-Y. Chen, and I.-M. Chen, "Magnetic field of tubular linear machines with dual halbach array," *Prog. Electromagn. Res.*, vol. 136, pp. 283–299, 2013.

[11] K. J. Meessen, J. J. H. Paulides, and E. A. Lomonova, "Analysis of 3-D effects in segmented cylindrical quasi-halbach magnet arrays," *IEEE Trans. Magn.*, vol. 47, pp. 727–733, Apr. 2011.

[12] M. Abramowitz and I. A. Stegun, Eds., *Handbook of Mathematical Functions with Formulas, Graphs, and Mathematical Tables*, 10th ed. New York: Dover, 1964.

[13] J. Wang and D. Howe, "Design optimization of radially magnetized, iron-cored, tubular permanent-magnet machines and drive systems," *IEEE Trans. Magn.*, vol. 40, pp. 3262–3277, Sep. 2004.

[14] K. J. Meessen, B. L. J. Gysen, J. J. H. Paulides, and E. A. Lomonova, "General formulation of fringing fields in 3-D cylindrical structures using Fourier analysis," *IEEE Trans. Magn.*, vol. 48, pp. 2307–2323, Aug. 2012.

[15] User israelkk. (2005, Aug. 29) B-H curve for 1018 steel. Eng-Tips Forums. [Online]. Available: http://www.eng-tips.com/viewthread.cfm?qid=132964